

Article

Reconstruction of Pressureless Sintered Micron Silver Joints and Simulation Analysis of Elasticity Degradation in Deep Space Environment

Wendi Guo ¹, Guicui Fu ¹, Bo Wan ^{1,*} and Ming Zhu ²

¹ School of Reliability and Systems Engineering, Beihang University, Beijing 100191, China; gwd14141068@buaa.edu.cn (W.G.); fuguicui@buaa.edu.cn (G.F.)

² China Academy of Space Technology, Beijing 100094, China; baofan33@gmail.com

* Correspondence: wanbo@buaa.edu.cn; Tel.: +86-156-5292-8449

Received: 22 July 2020; Accepted: 9 September 2020; Published: 12 September 2020



Featured Application: It is a hot topic to find green adhesive materials to adapt to the deep space environment. Due to its economy, excellent electrical and thermal conductivity and mechanical properties, pressureless sintered micron silver paste has great application potential in the aerospace field. Several reliability issues with this material are mainly focused on its high temperature stability, while the microstructural evolution and macroscopic performance in the harsh deep space environment have not been considered. Moreover, the inevitable existence of pores caused by the specific sintering mechanism will significantly affect the performance of joints and result in potential reliability problems, and the relationship is not easily tested. Therefore, using a cost-effective method to study this relationship is necessary to promote its reliable applications. In this work, we design a test profile to stimulate the deep space environment, develop a simplified reconstruction and simulation methodology and quantitatively evaluate the elastic performance of joints. Furthermore, we also present the mechanism by which microstructural evolution has a negative impact on elastic mechanical performance in this environment.

Abstract: With excellent economy and properties, pressureless sintered micron silver has been regarded as an environmentally friendly interconnection material. In order to promote its reliable application in deep space exploration considering the porous microstructural evolution and its effect on macroscopic performance, simulation analysis based on the reconstruction of pressureless sintered micron silver joints was carried out. In this paper, the deep space environment was achieved by a test of 250 extreme thermal shocks of $-170\text{ }^{\circ}\text{C}\sim 125\text{ }^{\circ}\text{C}$, and the microstructural evolution was observed by using SEM. Taking advantage of the morphology autocorrelation function, three-dimensional models of the random-distribution medium consistent with SEM images were reconstructed, and utilized in further Finite Element Analysis (FEA) of material effective elastic modulus through a transfer procedure. Compared with test results and two analytical models, the good consistency of the prediction results proves that the proposed method is reliable. Through analyzing the change in autocorrelation functions, the microstructural evolution with increasing shocks was quantitatively characterized. Mechanical response characteristics in FEA were discussed. Moreover, the elasticity degradation was noticed and the mechanism in this special environment was clarified.

Keywords: pressureless sintered micron silver joints; deep space environment; extreme thermal shocks; reconstruction; simulation; elastic mechanical properties

1. Introduction

In a deep space environment, the exploration equipment with complex electric systems suffers from extreme thermal shocks, inducing material performance degradation and further leading to the failure of electronic packaging. The reasons could be clarified by the research on the reliability of Sn/Pb and SnAgCu solder packaging which shows vulnerability to thermal shocks of Pb-free solders and Sn/Pb solders [1,2]. Therefore, finding alternative green bonding materials to adapt to the space environment has become an urgent research hotspot. Considering its outstanding ability to withstand heat, power, and stable mechanical properties [3–5], the sintered silver material has broad potential applications in harsh environments. However, compared to nano-silver particles [6–8], the pressureless sintered micron silver is affordable but is given less attention.

To reliably put it into use in deep space, the study of mechanical properties and the possible degradation mechanism of pressureless sintered micron silver joints in a deep space environment is valuable. Due to specific sintering mechanisms, randomly distributed pores inevitably exist in the microstructure of sintered joints [9], which will significantly affect material properties (i.e., the mechanical, thermal properties, etc.) and lead to possible reliability problems. The published studies drew the conclusion that Spherical and cylindrical voids had a significant effect on the thermal resistance of CSP packages [10], and an increase in void rate could result in a decrease in the shear strength of the solder layer [11], and voids would greatly shorten the fatigue life due to reduction in the overall carrying capacity [12]; these studies all established regular pore models and applied different pore locations and distribution rates. This kind of simulation study is mainly used to analyze the relationship between the microstructure and macroscopic performance of the porous adhesive layer because of costly and technically demanding experiments. However, the pores were simplified to the circle or column shape regardless of the actual shape in these simulations, so the corresponding results could be less accurate. For obtaining precise results, other researchers worked to link real microscopic structures of sintered silver with the properties. T. Youssef [13] reconstructed the 3D model of a sintered sample by utilizing a focused ion beam–scanning electron microscope (FIB–SEM) and the software AVIZO, and analyzed the changing trend of thermal and mechanical properties with increased porosity, which required a large number of high-accuracy serial slice images. X. Milhet [14] obtained elastic constants of sintered joints by applying dynamic resonant testing to sintered bulk specimens which were produced to represent the real structure, but this needed large expenditure.

In order to reconstruct the microstructure of sintered silver and predict its properties in an economical, precise and practical way, the correlation function method based on the probability and mathematical statistics theories is introduced. Correlation functions have been developed to describe random heterogeneous materials, including n-point correlation functions, surface correlation functions, the linear path function, chord-length density function and so on [15]. Among them, n-point correlation functions can take the shape, distribution, and orientation of material components into consideration, and have shown themselves to be feasible in the numerical simulation of isotropic and anisotropic media, where n represents the order of functions. With a higher order, n-point correlation functions could provide more precise characterization of heterogeneous microstructures [16–18], but the technique of obtaining the optimum approximation with effective, unbiased, and accurate experimental estimation from projected images is not yet mature. The second order correlation function (two points) has successfully reconstructed porous media such as concrete [19], Berea sandstone [20] and other composites [21,22], whilst retaining the microstructural features. However, few simulations studying the microstructure of micron silver sintered joints which have similar porous morphology to the above materials and their relationship with mechanical properties based on this method have been performed, as a result of complex calculations and lacking of an approach to transfer the reconstructed models into Finite Element Analysis models.

To solve the above problems, a thermal shock test of $-170\text{ }^{\circ}\text{C}$ – $125\text{ }^{\circ}\text{C}$ is conducted to simulate the deep space environment, and the section morphology are obtained for further study. A simplified reconstruction method of pressureless sintered micron silver joints is presented and used in simulation

analysis of elasticity degradation, which is a key parameter to evaluate mechanical properties in the deep space environment. The rest of this paper is organized as follows: Section 2 describes the designed thermal shock test and sample information simulating the real package structure, as well as SEM image acquisition required for modeling. Section 3 presents detailed methods of the morphology characterization and reconstruction of joints and proposed simulation procedure, and then verifies these methods with relative entropy, analytical models and test results. Section 4 analyzes the microstructure evolution during extreme thermal shocks, and the mechanical response characteristics, and discusses the negative effect of microstructure on elastic properties of joints. Finally, in Section 5, the concluding remarks are stated.

2. Experiments

2.1. Die Attachment Samples

As shown in Figure 1a, the polished side of a square silicon die (5 mm × 5 mm × 1 mm) was coated with a 50 nm Ti and a 50 nm Ag metallization layer using magnetron sputtering technology. A Ti layer was used as an adhesive by reacting it with natural oxides on the wafers, and an Ag layer provided a covering layer for tight integration with sintered micron silver paste. For the die bonding substrate (10 mm × 10 mm × 2 mm), copper (Cu 99.9%) was selected to make it, and a 50 nm Ti layer designed to prevent oxidation and copper atoms from spreading to sintered Ag joints was sputtered on one side, followed by a 2 μm Ag layer. The sandwich structure of the die attachment sample is shown in Figure 1b, where the die attachment structure was the micron silver paste with a thickness of 100 μm. The sample was assembled by brushing the paste on the metallized substrate, placing the silicon wafer on the Ag paste with tweezers, and sintering in air at the temperature of 230 °C without pressure, as shown in Figure 1c.

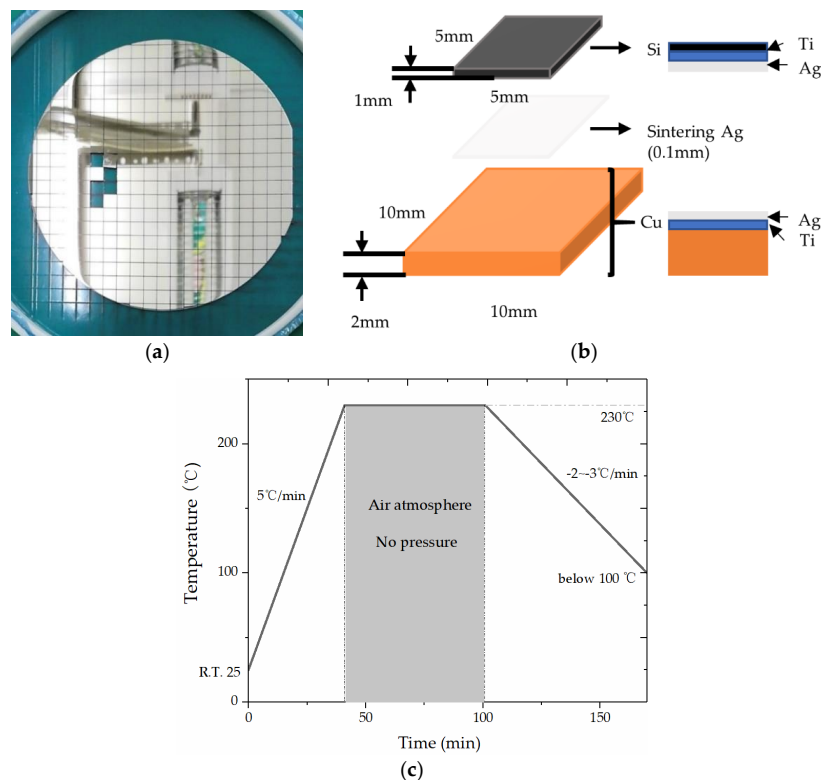


Figure 1. Details of die attachment samples: (a) Ti/Ag plated silicon dies; (b) the die attachment structure consisting of a Cu substrate, micron silver paste and one side polished die; (c) the curing process of micron silver joints.

Material parameters of the micron silver paste are listed in Table 1, and the SEM image with spectrum spot and EDS analysis result are shown in Figure 2. It can be seen that the material consists of submicron silver particles and silver flakes and involves the negligible carbon content which shows a small peak.

Table 1. Parameters of the pressureless sintered micron silver material.

Parameter	Condition	Micron Ag Paste
Ag content (wt%)	in paste	92–94
Viscosity, E-type 3° cone (Pa·s)	5 rpm@RT	18–22
Thixotropic Index	0.5 rpm/5 rpm	6.5
Volume Resistivity ($\Omega\cdot\text{cm}$)		5×10^{-6}
Poisson's ratio		0.25
Density (g/cm^3)		7.8
Elastic modulus (GPa)	Nanoindentation@RT	25
CTE ($\text{ppm}/^\circ\text{C}$)	Isotropy	18

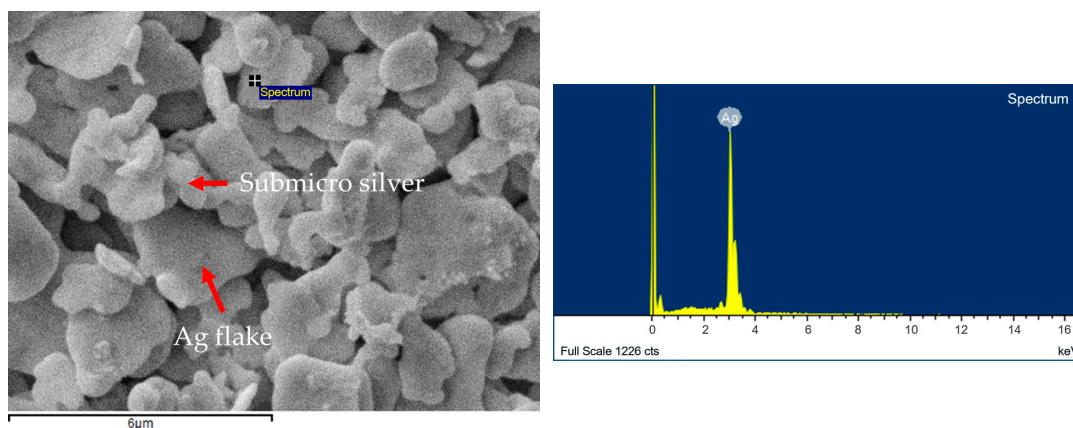


Figure 2. SEM image with spectrum spot and EDS analysis.

2.2. Thermal Shock Test

The drastic change of ambient temperature in deep space missions is an important factor resulting in internal defects in the packing of electronic devices. In order to study the mechanical properties of this new bonding material in space missions, a thermal shock test was carried out to simulate the aerospace environment, in which the temperature changed from -170°C to 125°C covering the temperature range of the moon, Mars, common asteroids and comets. During the test, samples were placed in a high and low temperature chamber with a thermal shock profile (Figure 3). The soak time of extreme temperature was 15 min, and the frequency was about 30 min/cycle.

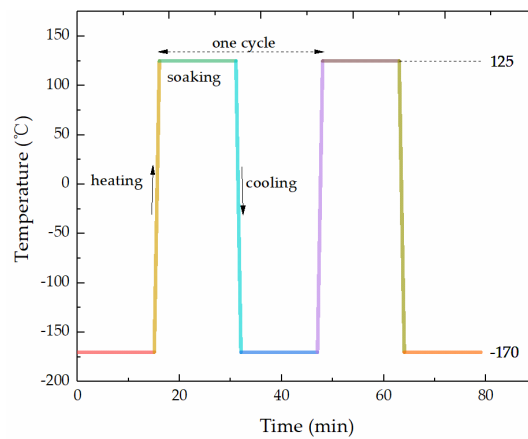


Figure 3. Thermal shock profile for the test application.

2.3. SEM Images of Micron Silver Sintered Joints

Prior to the thermal shock test, the die shear strength test was conducted to evaluate bonding strength and the reliability of bonding at the interfaces. The average shear strength of the sintered micron silver samples was 15 ± 2 Mpa, which showed good bonding quality. During the shearing process, a fracture almost occurred through the adhesive layer, indicating the reliability of bonding at the interfaces. However, there was still delamination occurring at the interface between the micron silver paste and the substrate, as seen in Figure 4. This was related to defects in the metallized layer. Samples that failed in such way in the further thermal shock test needed to be removed to focus on the adhesive layer performance degradation.

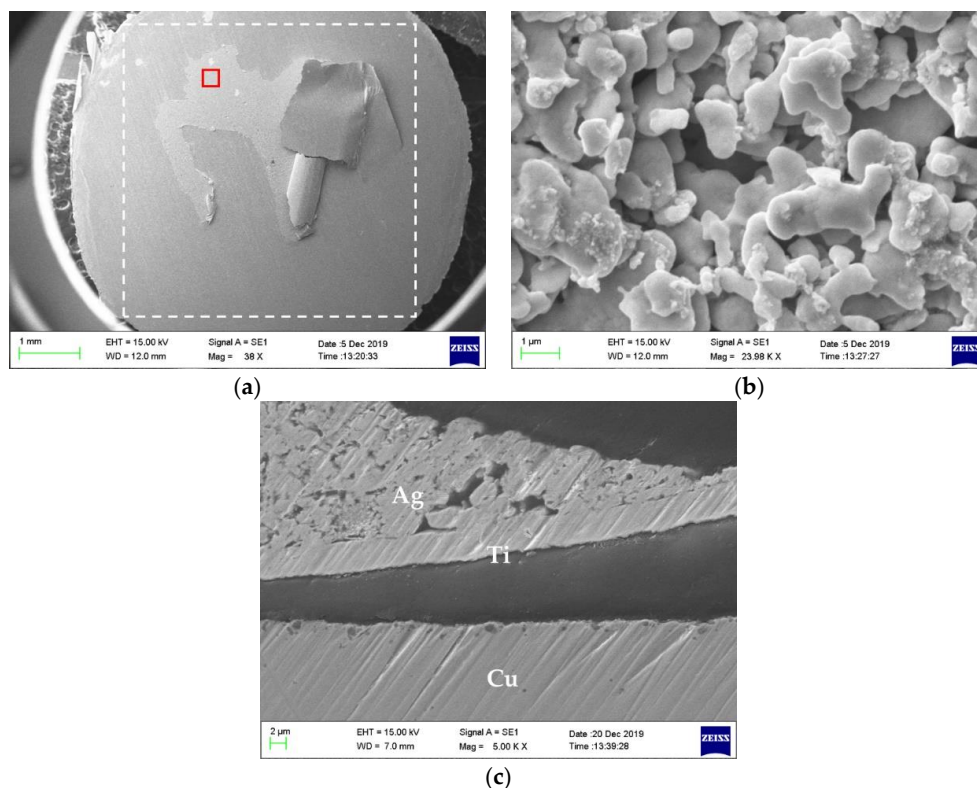


Figure 4. SEM images of the fracture of a micron silver joint after shear testing. The white frame represents the die position: (a) fracture occurs at the substrate–joint interface; (b) larger view of micron silver particles coalescing from selected red region in (a); (c) the metallized layer is separated from the substrate.

Sintered silver joints are characterized by a typical porous structure. Samples were taken out and molded every few thermal shocks. After longitudinal grinding, two-dimensional (2D) images of micron silver sintered joints were obtained by observing the microscopic morphology and shown in Figure 5, which were used as the initial data for three-dimensional (3D) reconstruction. No significant cracks were found in destructive tests.

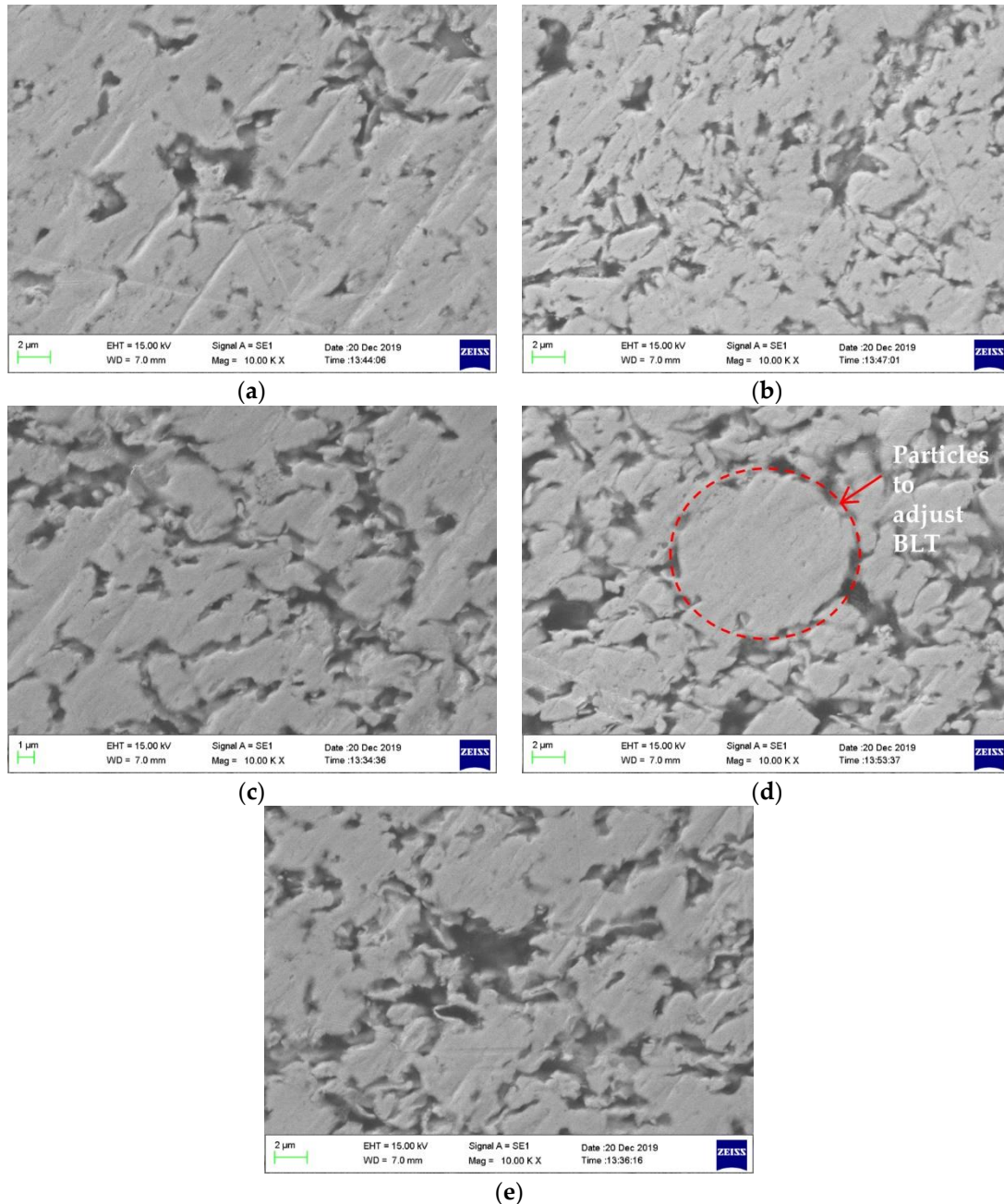


Figure 5. SEM images of micron silver sintered joints under thermal shocks for: (a) 0; (b) 50; (c) 100; (d) 150; and (e) 250 cycles.

3. Model Reconstruction and Finite Element Analysis

3.1. Structural Characterization and Reconstruction (SCR)

The Joshi Quiblier Adler (JQA) method [23] is a morphology autocorrelation-function-based tool for reconstructing porous media. To study the relationship between microstructure and performance

of micron silver sintered joints from a microscopic perspective, the method was simplified and used to characterize 2D cross sections and reconstruct a two-phase heterogeneous 3D model to provide the high-dimensional point cloud data required for simulation. During reconstruction, a Gaussian random field was used to generate spatial media, and the morphology and dispersion of two-phase interface were described by autocorrelation function. A region-based image segmentation technique iteratively solved the porosity of 3D models which was consistent with original images, and these models were corrected by smoothing operation. The whole flow is illustrated in Figure 6.

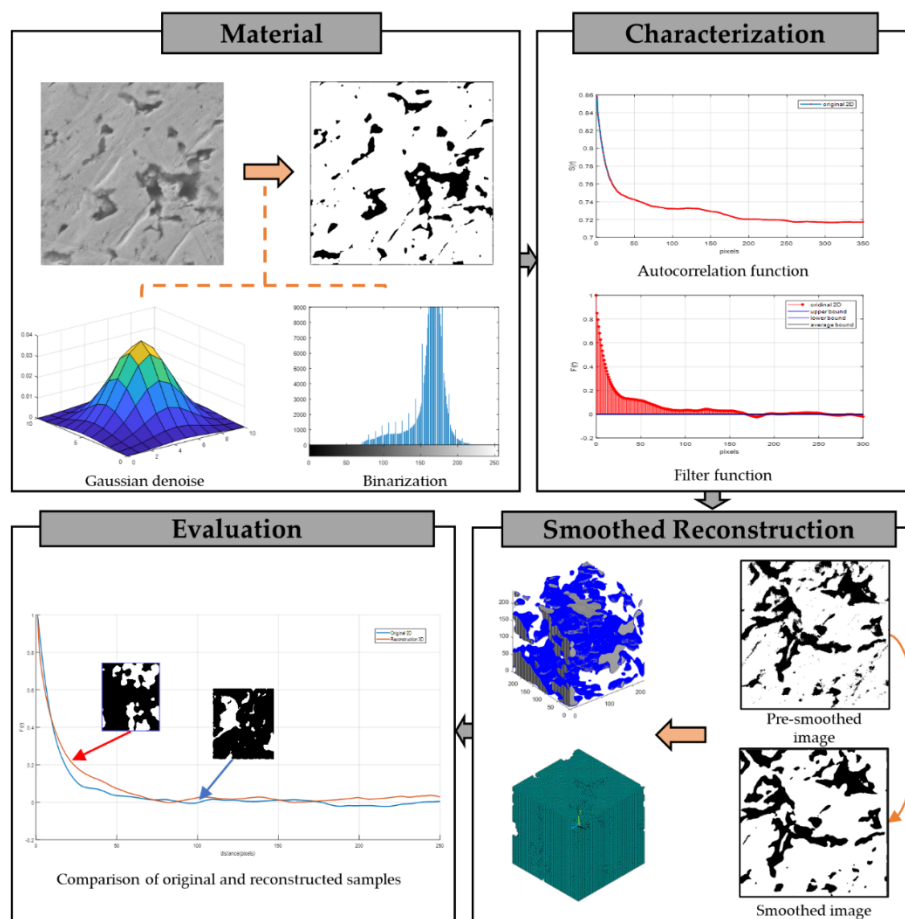


Figure 6. The Flow chart of reconstructing stochastically equivalent 3D morphology of sintered micron silver joints.

There are four main steps required to reconstruct the randomly distributed medium from an SEM picture using SCR, which are given below:

1. Denoising, threshold segmentation and binarization processing are applied on the original image to get the two-phase random medium, which is expressed as $V(\omega) \in \mathbb{R}^3$, a spatial domain. Where ω is the domain intercepted from the probability space of volume V , including two parts: the pore volume fraction φ_1 in the region V_1 and the volume fraction of micron silver particles φ_2 in the region V_2 . Binary porous media may be represented by an indicator function $I(x)$, as defined below:

$$I(x) = \begin{cases} 1, & x \in V_1 \\ 0, & x \in V_2 \end{cases} \quad (1)$$

2. The two-point autocorrelation function $S_2(r)$ is used to describe the morphology as shown in Equations (2) and (3). $S_2(r)$ is defined as follows: two arbitrary points, x_1 and x_2 of the distance r ,

are selected in an observation region, and the probability that both points are in one phase is $S_2(r)$, which is illustrated in Equation (4). For the isotropic material in this study, it can be calculated by bilinear interpolation [24].

$$S_2^i(r) = \langle I^i(x_1)I^i(x_2) \rangle = P\{I^i(x_1) = 1, I^i(x_2) = 1\}, \tag{2}$$

$$\begin{cases} S_2^i(r) = \phi_i, r = 0 \\ \lim_{r \rightarrow \infty} S_2^i(r) = \phi_i^2 \end{cases} \tag{3}$$

$$S_2(r) = \frac{\sum_{(m,n) \in \Omega} \left[\sum_{i=1}^M \sum_{j=1}^N I_{i,j} I_{i+m,j+n} \right]}{\omega MN}, \tag{4}$$

where ω is the number of elements in the set Ω which is calculated in Equation (5):

$$\Omega = \{(m, n) | m^2 + n^2 = r^2, r \leq [\min\{M, N\}/2]\}. \tag{5}$$

The normalized autocorrelation function in the spherical coordinate, as Equation (6), is used as the filtering function of normally distributed noise:

$$F(R) = \frac{E\{[I^i(x + R) - \phi_i] \cdot [I^i(x) - \phi_i]\}}{E\{[I^i(x) - \phi_i]^2\}}. \tag{6}$$

3. X_1 and X_2 are uniformly distributed random numbers. Based on Box–Muller, these two random numbers can be used to generate Gaussian-distributed noise N efficiently, with a mean of 0 and a variance of 1, as shown in Equation (7).

$$N = \sqrt{-2 \ln X_1} \cos(2\pi X_2), X_1 \sim U(0, 1), X_2 \sim U(0, 1). \tag{7}$$

As shown in Equation (8), the initial 3D image with Gaussian noise can be obtained:

$$I(i, j, k) = \sum_{r,s,t} N(r, s, t) \times F(i + r, j + s, k + t). \tag{8}$$

According to Equation (9), iterative threshold segmentation is performed on 3D images to match the porosity of SEM pictures. The Fourier transform is used to perform three-dimensional Gaussian smoothing operation to correct reconstructed 3D models, which is calculated as Equation (10). Finally, high-dimensional binary matrix is then obtained:

$$porosity(\%) = \frac{\sum_{\substack{1 \leq i \leq M \\ 1 \leq j \leq N}} I_{i,j}^{(V_1)}}{MN} \times 100\%, \tag{9}$$

$$f(x, y, z) = 2\pi^{-\frac{3}{2\sigma^3}} \exp\left(-\left(\frac{2x^2}{\sigma^2} - \frac{2y^2}{\sigma^2} - \frac{2z^2}{\sigma^2}\right)\right). \tag{10}$$

4. Kullback–Leibler (KL) divergence, also known as relative entropy, is a measure of the difference between two distributions P_1 and P_2 to evaluate the reconstruction quality, as shown in

Equation (11). The KL divergence is calculated from 0 to $+\infty$, indicating the similarity from the most to the least.

$$KL(P_1||P_2) = \sum_{x \in X} P_1(x) \log \frac{P_1(x)}{P_2(x)}. \tag{11}$$

Through the above process, a series of high-dimensional data equaling to the 3D geometry reconstructed model could be obtained and transferred into the Finite Element Analysis (FEA) model as below. The high-dimensional data can be discretized and reduced into a set of unit information, called volume data. These data logically form a 3D array space, and each array point stores volume location and feature information, called a voxel. The location of one voxel was determined by layer, row and column, as shown in Figure 7a. Voxels belonging to the medium are marked as $v = 1$, and those belonging to the pore are marked as $v = 0$. The thin layer of volume data is shown in Figure 7b. All voxels' information is stored in a TXT file and imported in the ANSYS Parametric Design Language (APDL) program to build the 3D entity in ANSYS Mechanical for FEA, which is a Boolean description of micron silver sintered material with voxels as units in space. The voxel is built by 8 key-points illustrated in Figure 7c, where i, j and k represent the voxel location coordinate, respectively.

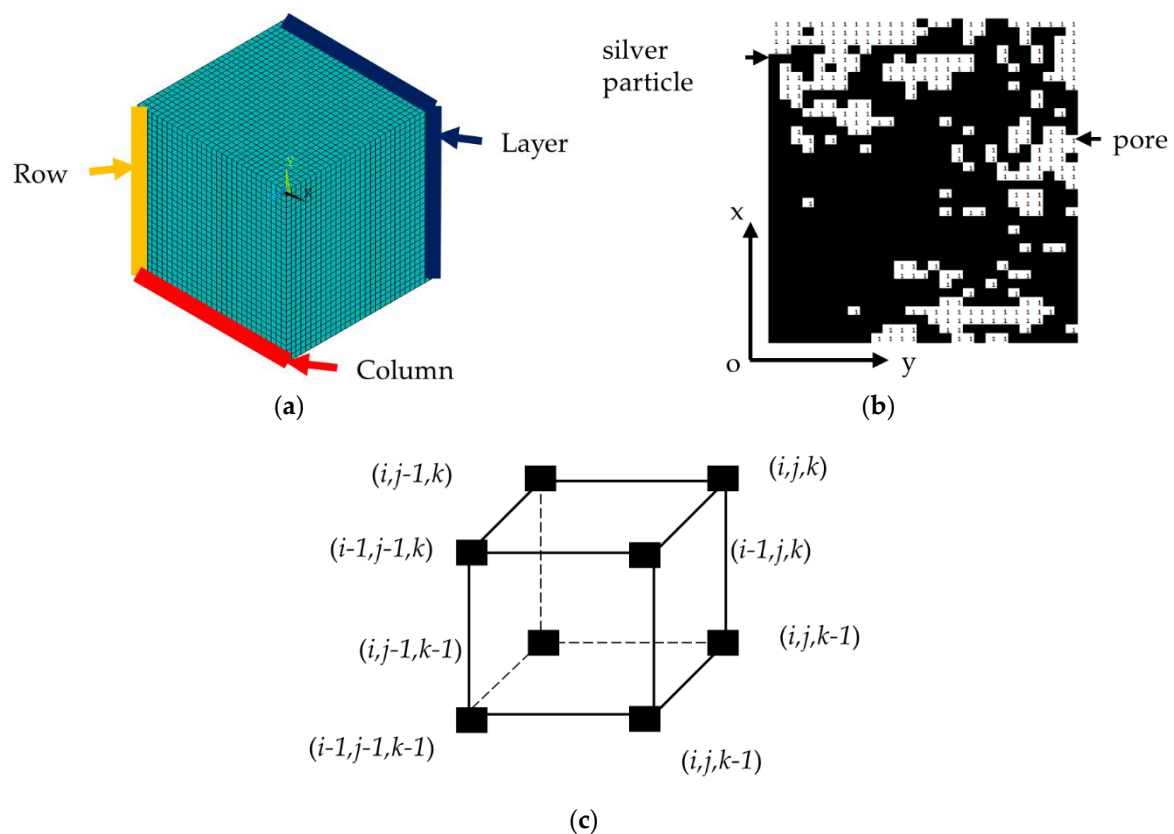


Figure 7. Indication of spatial data. (a) Spatial volume data; (b) A thin-layer model; (c) One voxel built in ANSYS Mechanical.

Without considering the effect of the grain boundary of fused micron silver particles, reconstructed models of joints can be obtained by reverse filling the pores with Boolean operation. Reconstructed pore visualization results and 3D FEA models corresponding to SEM images of micron silver sintered joints under different thermal shocks are shown in Figure 8.

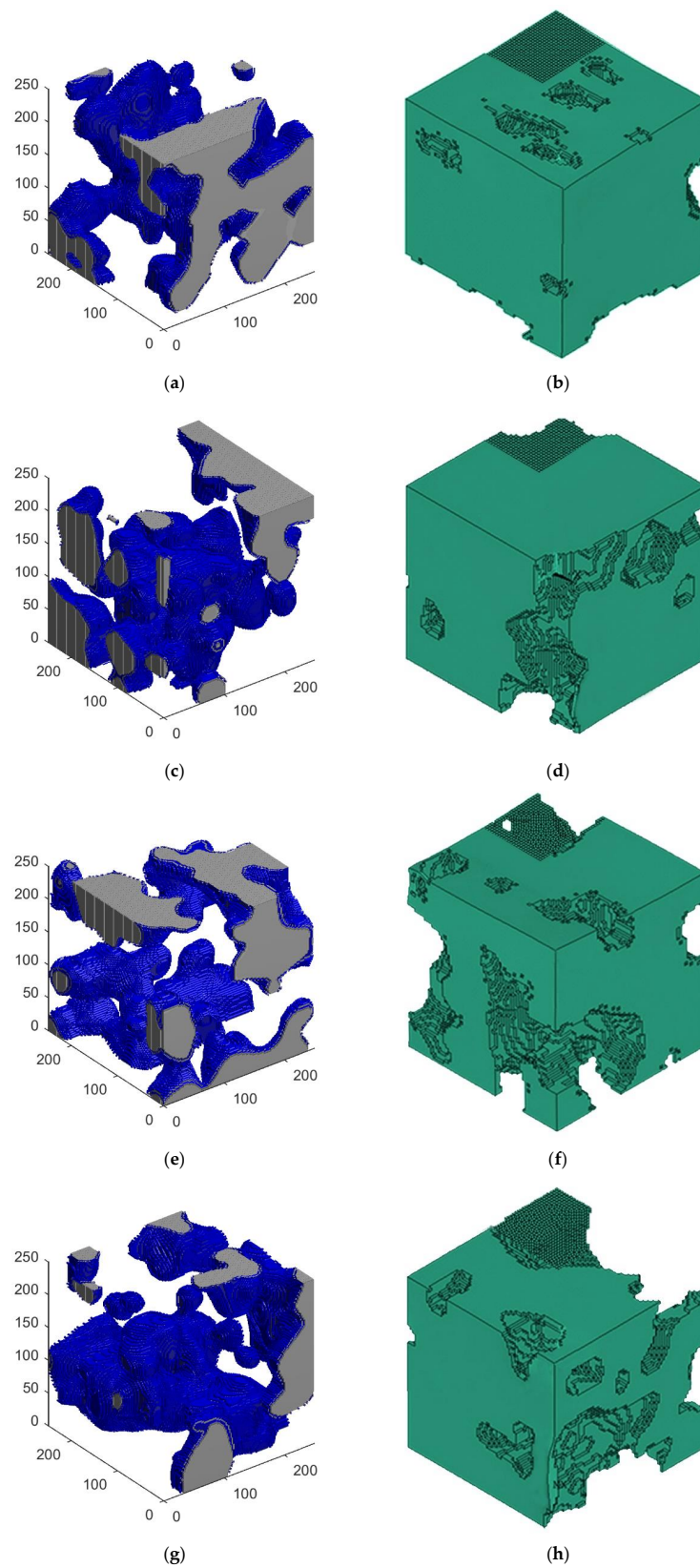


Figure 8. Reconstructed pore topological structures and 3D Finite Element Analysis (FEA) models with mesh in a small area corresponding to SEM images of micron silver sintered joints under different thermal shocks: (a,b) 50; (c,d) 150; (e,f) 150; (g,h) 250 cycles. In 3D views of the left column, gray represents defined geometric boundaries, and blue is the iso-surface.

Normalized autocorrelation functions of SEM images and 3D reconstruction models are plotted in Figure 9, where the size of reconstructed models (250 pixels) is much larger than the observed correlation length of SEM samples (the autocorrelation function asymptotic location), illustrating reconstructed models can represent the microstructure of sintered joints. The KL divergence values are calculated and listed in Table 2, which are within an acceptable range (less than 15%). Both qualitative observation and quantitative calculation show that the reconstructed models are consistent with the original images.

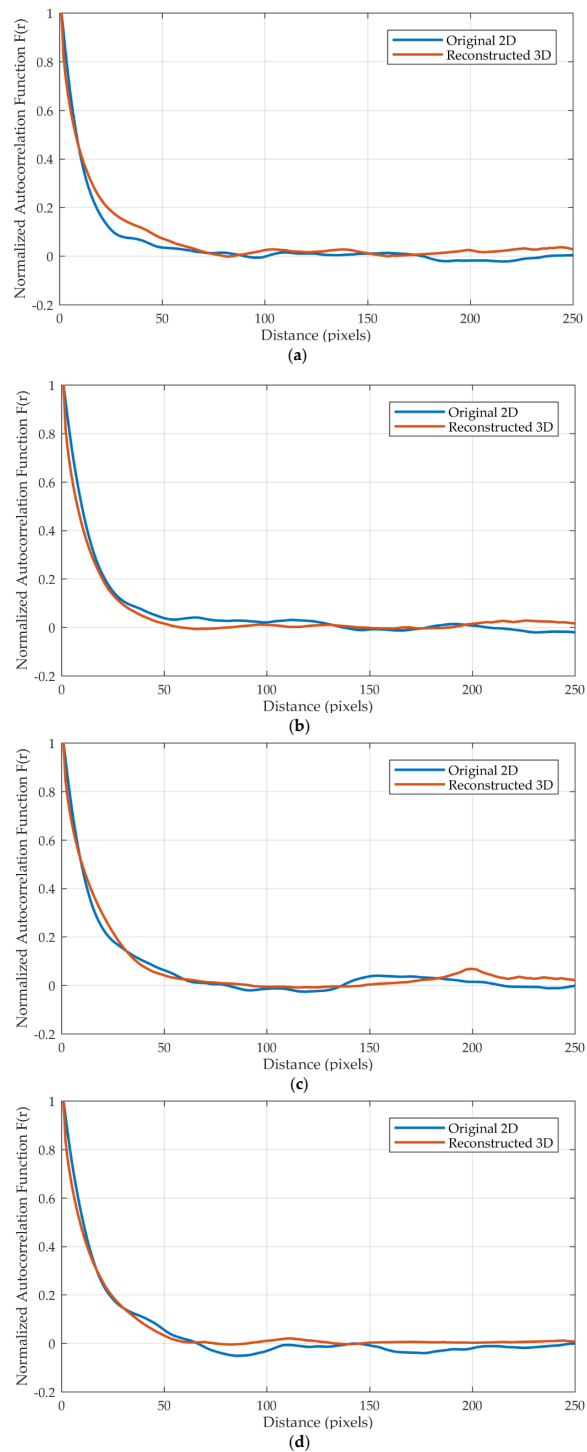


Figure 9. Comparison of autocorrelation functions of SEM images and 3D reconstruction models with thermal shock cycles are (a) 50; (b) 100; (c) 150; (d) 250.

Table 2. Kullback–Leibler (KL) divergence between autocorrelation functions.

Thermal Shock (Cycles)	50	100	150	250
KL divergence	0.11	0.12	0.12	0.08

3.2. FEA Simulation

To obtain the effective elastic modulus value of the micron silver sintered joints under thermal shock, the simulation loading conditions were set as below: one side of the reconstructed model was subjected to a fixed constraint and the opposite side was put into stress σ_i , shown in Figure 10. The input Young’s modulus was set from nanoindentation result of 25 Gpa. The density and the Poisson’s ratio were 7.8 g/cm³ and 0.25. For the FEA model with length L , the displacement on the force surface and equivalent stress of each node are extracted, and the effective elastic modulus is calculated by Equations (12) and (13).

$$E_i = \frac{F_i L}{A x_i}, \tag{12}$$

$$E = \frac{\sum_i E_i}{n} = \frac{\sum_i \left[\sigma_{ave} / \left(\frac{dL_i}{L} \right) \right]}{n}, \tag{13}$$

where E_i is the effective elastic modulus obtained by fixing X, Y and Z planes, respectively, to eliminate the calculation error caused by structural randomness. F_i is tension, x_i is displacement and A is the section area. n is the number of simulation tests, and σ_{ave} is the average tensile stress which is calculated as Equation (14). dL_i is the average displacement in the stress direction.

$$\sigma_{ave} = \frac{\sum_i \sigma_i \times V_i}{V_{medium}}, \tag{14}$$

σ_i is the equivalent stress in the i^{th} node. V_i is the volume of element in which node i resides. V_{medium} is the total volume of all nodes in elements.

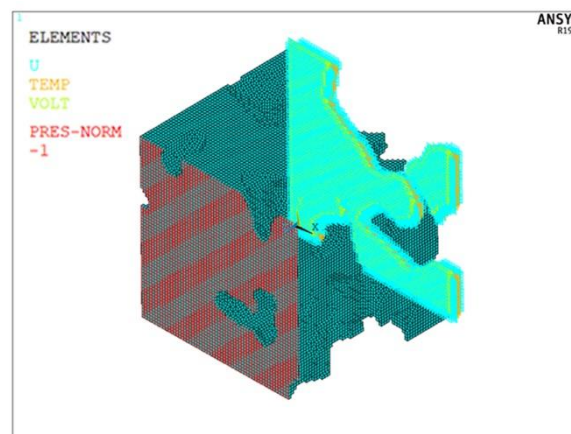


Figure 10. Simulation loading diagram. Green represents a fixed constraint, and red represents applied tensile stress. The element type is Solid 226.

The calculation of average stress can reduce the stress inequality caused by complex structure, which is equivalent to the effective stress of sintered joints. Moreover, it depends on the microstructural characteristics rather than stress concentrations of individual points.

Table 3 shows the model size, the number of elements and calculation time during simulation. After generating FE models, the solving process generally requires 20 to 30 min. The cumulative time

spent on modeling and meshing is relatively significant, about 3 h, so as to ensure the quality of these simulation models.

Table 3. Information about elastic modulus simulation.

Thermal Shock (Cycles)	Model Size (Pixels)	Number of Elements	Calculation Time (min)
50	250 ³	172,195	20 to 30
100		168,307	
150		160,390	
250		160,380	

The simulation results of displacement and equivalent stress are shown in Figures 11 and 12.

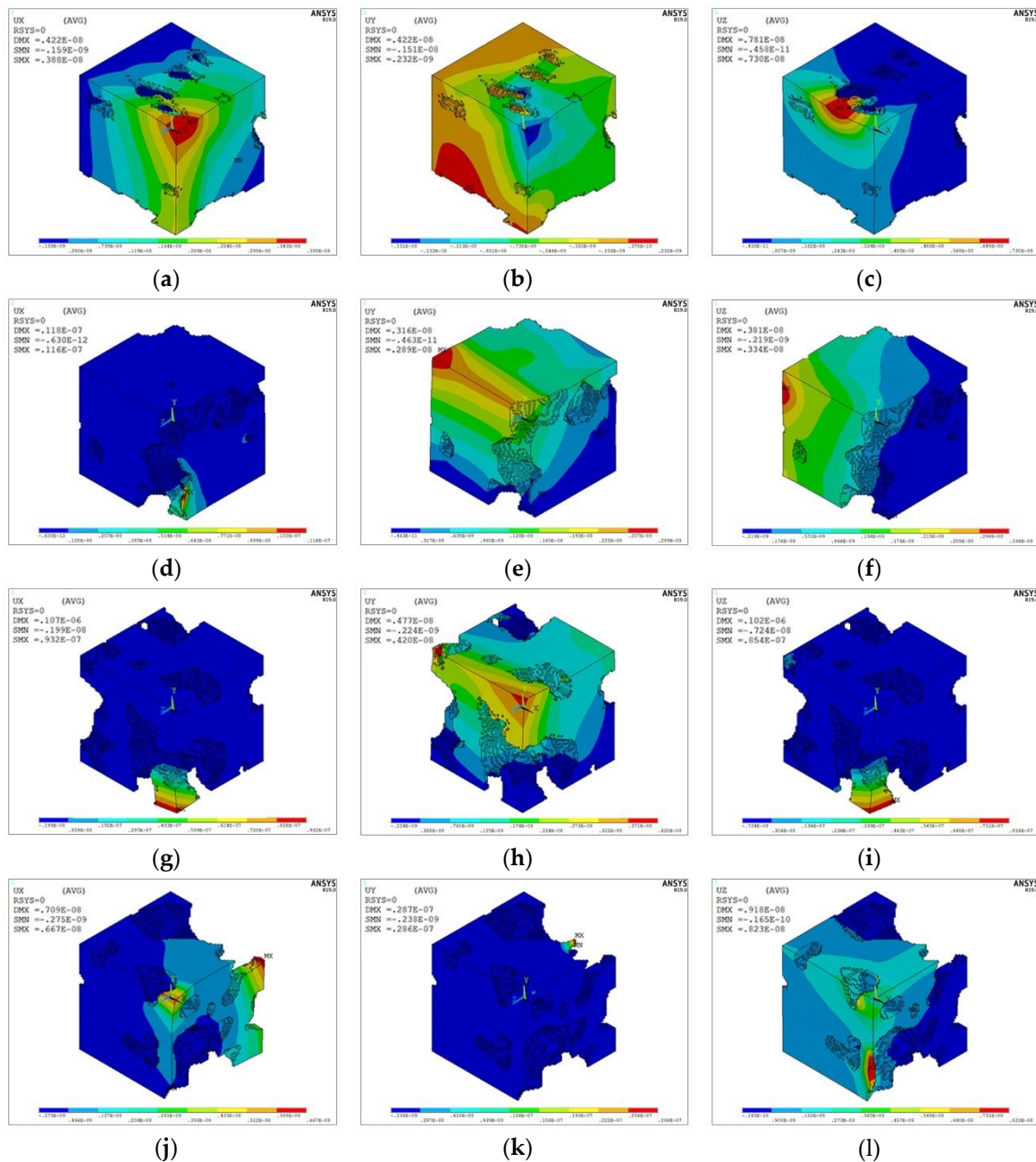


Figure 11. Displacement analysis results of micron silver sintered joints under different thermal shocks by fixing X, Y and Z planes, respectively: (a–c) 50; (d–f) 100; (g–i) 150; (j–l) 250 cycles.

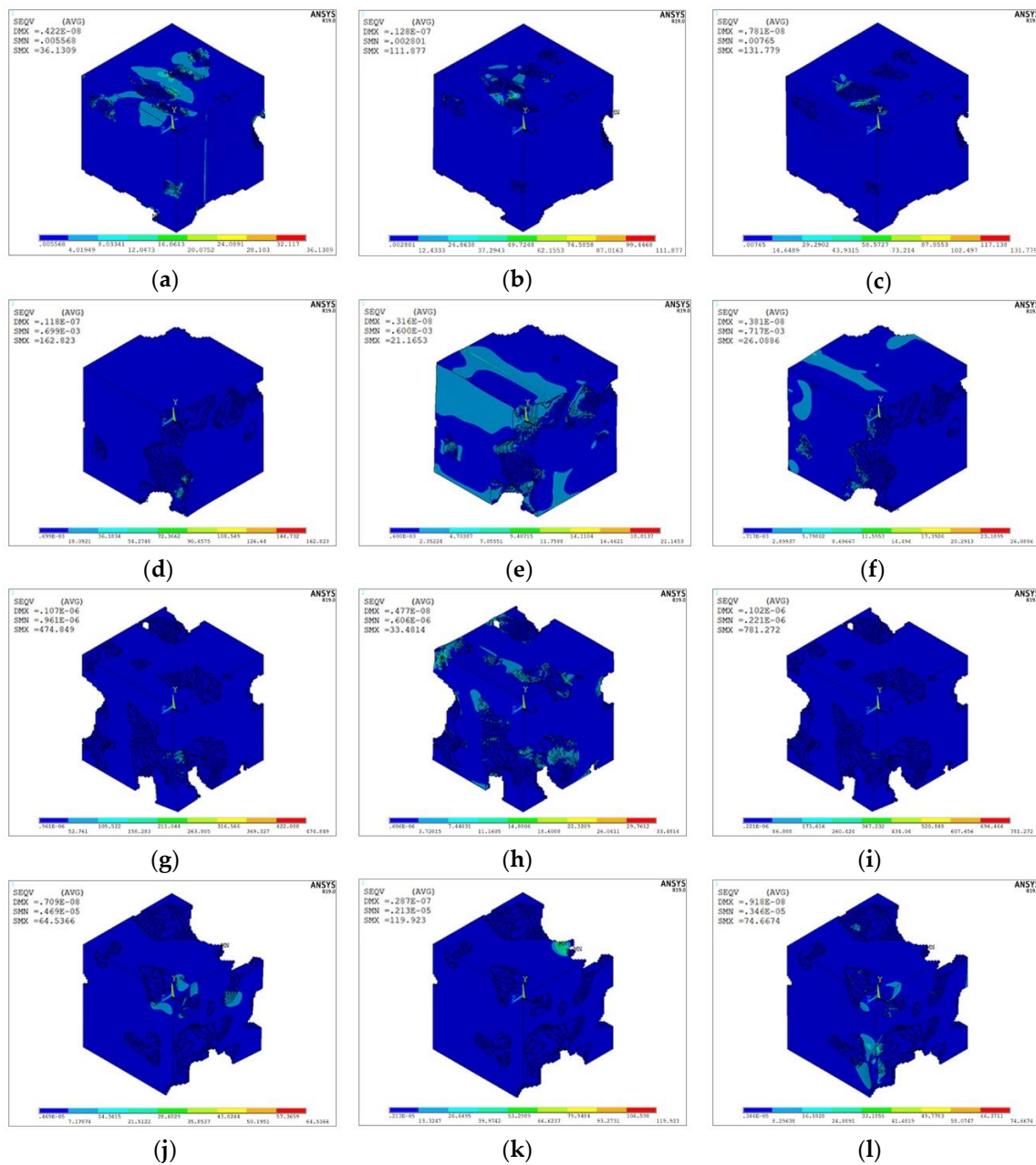


Figure 12. Equivalent stress analysis results of micron silver sintered joints under different thermal shocks by fixing X, Y and Z planes, respectively: (a–c) 50; (d–f) 100; (g–i) 150; (j–l) 250 cycles.

3.3. Analytical Model and Experimental Validation

The analytical model of the effective elastic constants of porous solids is based on numerical simulation and microstructure measurement, and it is considered to be a relatively accurate empirical equation for predicting elastic properties. In order to ensure the rationality of this simulation route and accurately quantify the microstructural damage on elastic properties of micron silver sintered joints, two analytical models were used to calculate the elastic modulus at different thermal shocks and these results were compared with simulation results. The first model corresponds to the Ramakrishnan and Arunachalam (R&A) method [25] and is conducted as Equations (15) and (16).

$$E_p = E_0(1 - p)^2 / (1 + b_p p), \quad (15)$$

$$v = \frac{1}{4} \frac{(4v_0 + 3p - 7v_0p)}{(1 + 2p - 3v_0p)}, \tag{16}$$

where, $b_p = 2$ to $3v$, p is the pore volume fraction. v_0, E_0 is the Poisson’s ratio and elastic modulus for undamaged material, and E_p is the elastic modulus corresponding to a certain damage state.

Another model, the modified value of porous materials (M) [26] in Equation (17) was used to estimate the effect of microscopic damage on elastic modulus. The parameter definition is the same as above.

$$E_p = E_0 - pE_0 \left(\frac{9 - 4v_0 - 5v_0^2}{7 - 5v_0} \right). \tag{17}$$

Furthermore, nanoindentation test was used to measure the load and corresponding displacement of pressureless micron sintered joints. The geometric vertices and center point of the silver welding layer were selected as test positions, and the average value was taken as the test result. If there is a large deviation in the above positions, it is determined that the silver bonding layer of the sample is uneven during sintering, and needs to be rejected. Meanwhile, a new sample is re-selected for testing. The designed stress curve is shown in Figure 13.

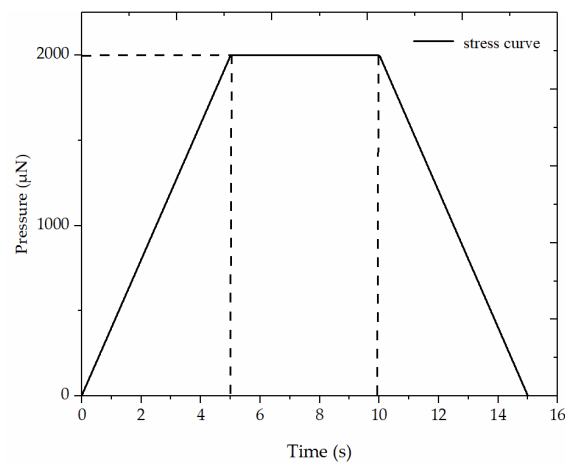


Figure 13. Applied nanoindentation stress curve.

For geometries based on SCR method, normalized calculation results of FEA and theoretical models and nanoindentation tests are plotted in Figure 14. The error among simulation and test and R&A method is within 15%, which indicates that the proposed simulation route and the elastic properties of micron silver sintered joints obtained by FEA are reliable and precise.

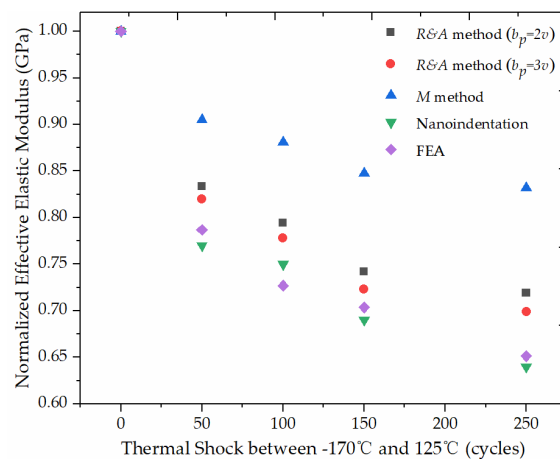


Figure 14. Relative comparison of FEA, analytical models and nanoindentation results.

4. Results and Discussion

4.1. Microstructural Evolution

The simulation illustrates that the effective elastic modulus degrades with the accumulation of shock cycles. In order to study the cause of performance degradation, the microstructural evolution is characterized from autocorrelation functions.

The specific surface, marked as s , of two-phase media is defined as the two-phase interface area per unit total volume, which can be obtained from the slope of the two-point autocorrelation function [27]. In this study, s of original images and reconstructed models is conducted from Equation (18):

$$\frac{d}{dr} S_2(r) \Big|_{r=0} = \begin{cases} -s/\pi, D = 2 \\ -s/4, D = 3 \end{cases} \quad (18)$$

Specific surface can be used to estimate the hydraulic diameter (D_H) of porous media [28], which is calculated in Equation (19). V is the volume fraction of the medium:

$$D_H = \frac{4V}{s} \quad (19)$$

The captured autocorrelation functions of original SEM images from Figure 5 changes with thermal shocks are shown in Figure 15. There is an increase in the slope at the origin and a decrease in the correlation length. Changes of the mean particle size, hydraulic diameter and specific surface in SEM pictures and reconstructed models are calculated as shown in Table 4.

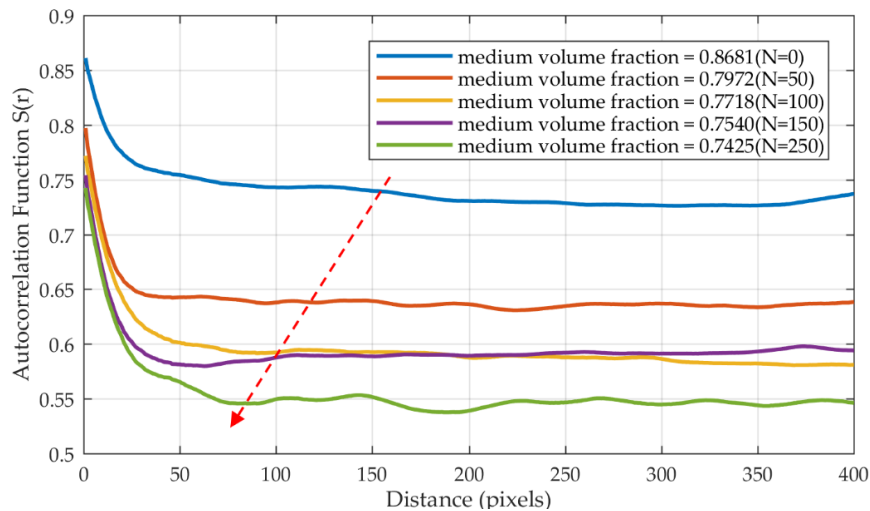


Figure 15. Autocorrelation functions under the accumulation of thermal shocks.

Table 4. The particle size, hydraulic diameter and specific surface of original images and reconstructed models.

Thermal Shock (Cycles)	$D_{P,2D}$ (μm)	$D_{P,3D}$ (μm)	$D_{H,2D}$ (μm)	$D_{H,3D}$ (μm)	s_{2D} (μm^{-1})	s_{3D} (μm^{-1})
0	4.30	-	3.16	-	1.10	-
50	3.03	2.88	1.88	2.03	1.70	1.57
100	2.24	2.12	2.25	2.16	1.37	1.43
150	1.91	1.82	2.15	2.05	1.40	1.47
250	2.03	1.97	1.98	1.86	1.50	1.60

It can be seen that the average micron-silver particle size decreases, while this is in contrast to a slight increase in the size of silver grains ($-45\text{ }^\circ\text{C}\sim 250\text{ }^\circ\text{C}$) reported in [29]. It should be noted that the surface diffusivity of silver is relatively lower at $125\text{ }^\circ\text{C}$ [30] than the melting point and

sintering temperature. Meanwhile the soak of $-170\text{ }^{\circ}\text{C}$ seems to prevent particle recrystallization growth and even reverse-driven particles from dispersing. The hydraulic diameter of the medium declines with fluctuation. If the porous medium is regarded as an interconnected pipeline network, the above situation can be interpreted as the rise of pore density and pore nucleation growth induced by cyclic loading, which is consistent with the measured increase in average pore size and porosity [31]. The whole tendency of the specific surface goes up, which physically means that the total surface area of pores increases. The results demonstrate that damage gradually accumulates with thermal shock testing, resulting in the increase in porosity and the role of pores as grain growth inhibitors. The contact area between adjacent grains and the size of the medium decreases. The medium particles tend to disperse. In Figure 15 autocorrelation functions slightly oscillate after 50 thermal shocks, which reflects in the influence of the roundness of micron silver particles. Furthermore, another important finding from visual the view of pores (Figure 8) is that the pore distribution area becomes uneven and the local density changes, which will further promote the initiation of cracks.

4.2. Mechanical Response Characteristics

Extrema of mechanical response characteristics of nodal solutions in previous FEA simulation could be observed in Figures 11 and 12, which illustrate the displacement and stress of reconstructed micron silver sintered joints suffering different thermal shock cycles in the X, Y, and Z directions. It can be seen that the maximum and minimum values of the displacement and stress show a similar fluctuation in the X and Z directions with increasing thermal shocks. This is because the x–z plane represents the parallel interface of this sandwich structure, and the Y axis is the longitudinal constrained sintering direction, so there is a certain degree of anisotropy.

It can be found that the maximum displacement point appears near the junction of silver phase and larger pores, or the corner of pores, and the value shows an increasing trend, which demonstrates that the rise of porosity and particle dispersion caused by increased thermal shocks leads to the decrease in the size of the load-transmission area between particles, and can further result in a large displacement field across the local bearing surface. This situation also indicates that the elastic performance of micron silver sintered joints declines. On the other hand, the variation range of triaxial stress gradually increases as the thermal shock cycles increases. In addition, stress concentrations exist in all three directions. This situation could be explained by more likely stress concentrations resulting from the growing porosity.

Table 5 illustrates the triaxial elastic modulus and the effective elastic modulus by FEA, and the apparent density of samples. It can be seen that the Y-axis elastic modulus is a little greater than those of the X and Z axes. This phenomenon should be derived from the sample structure, and the constrained sintering state leads to a slight anisotropic microstructure [32]. Considering the slight degree of anisotropy, the effective elastic modulus is adopted to evaluate the degradation behavior of the micron sintered silver joints. As the thermal shock cycles increase, the apparent density of micron silver joints decreases, indicating that cyclic thermal stress can drop the material densification.

Table 5. The elastic modulus in three directions, the effective elastic modulus and apparent density.

Thermal Shock (Cycles)	E_X (GPa)	E_Y (GPa)	E_Z (GPa)	E_{eff} (GPa)	Apparent Density (g/cm^3)
50	19.63	20.70	19.50	19.94	7.46
100	17.60	20.98	19.08	19.22	7.22
150	16.31	18.12	17.52	17.32	7.05
250	16.22	16.92	15.56	16.24	6.93

4.3. Elasticity Degradation

Based on the data in Table 5, Figure 16 illustrates the change of effective elastic modulus and porosity of micron silver sintered joints with accumulated extreme thermal shocks. The porosity changes from 13.19% to 25.75% and the effective elastic modulus decreases by about 36%. Since the

elastic modulus of three axes is calculated with deviation among different directions, it can be concluded that the elastic properties of micron silver joints are also related to the microscopic topological structure. The closer the reconstruction is to the original, the less the simulation fluctuates.

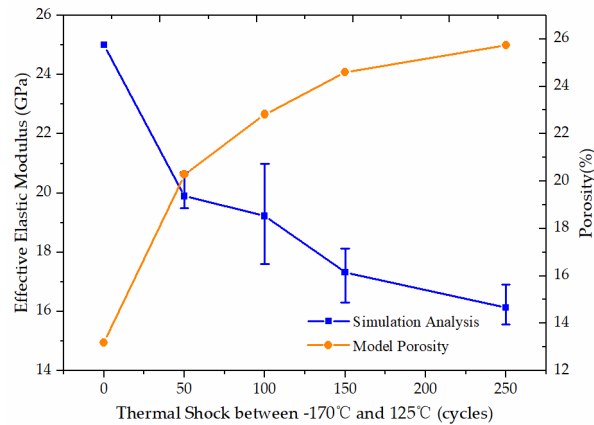


Figure 16. Changes in effective elastic modulus and porosity.

Compared with analytical predictions which only consider porosity as the main factor, it is found that FEA is close to the R&A method for solving the problem of modulus uncertainty by using the special model of the change of the effective Poisson’s ratio. However, the forecast is slightly larger. The large deviation of the M method may be related to the premise that the composite material consists of a continuous matrix phase with a high concentration of rigid spherical inclusion suspension. The comparison with the test results also indicates that FEA can easily realize the prediction of elastic properties in micron silver sintered joints. The calculation taking errors caused by structural randomness into account basically covers nanoindentation results (Figure 17).

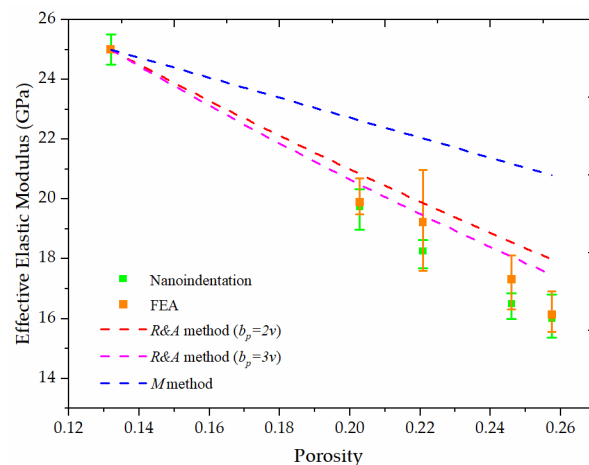


Figure 17. Effective elastic modulus degradation with porosity.

To clarify the elasticity degradation, a mechanism analysis is taken and discussed below. Micron silver atoms are held together by interaction and the elastic properties are directly related to the relative movement between atoms. Due to the mismatching of the thermal expansion coefficient of the sandwich structure, the adhesive layer is mainly subjected to shear force in the deep space environment regarding approximately monotonic loading. This may lead to lattice shift and dislocation slip in the microstructure (Figure 18).

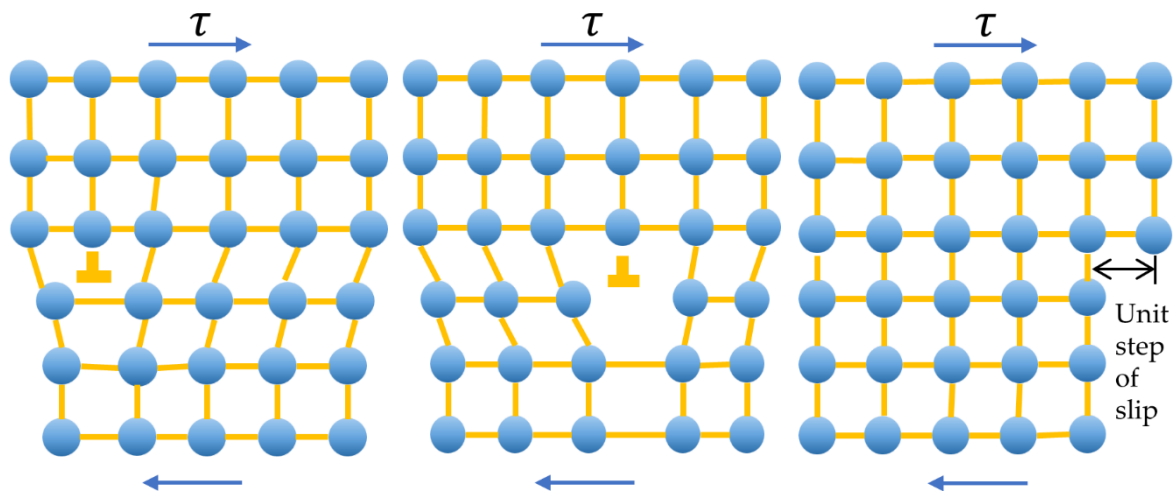


Figure 18. Dislocation from the perspective of a slip plane.

If the dislocation stops due to the concentration of micro-stress in sintered silver joints, a constrained region will be formed, where other dislocations may stop. At this time, the subsequent dislocation of the same dislocation increment occurs, piling up as shown in Figure 19. This defect can cause a decreasing number of atomic bonds; consequently, the effective elastic modulus shows degradation. Moreover, this defect can be observed as the growth of pores and dispersion of silver grains.

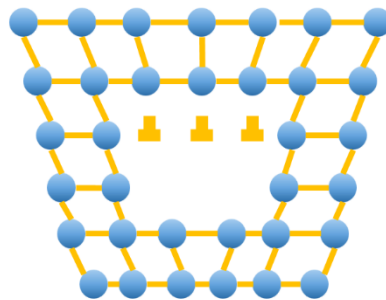


Figure 19. Ductile dislocation piling up.

5. Conclusions

This study is undertaken to provide a cost-effective modeling and simulation method for the elastic mechanical properties of pressureless micron silver sintered joints based on microstructure reconstruction and analyzing the cause of its elasticity degradation in a deep space environment. The following conclusions are drawn:

- (1) A simplified statistical reconstruction method based on JQA is proposed, which takes the random morphology and distribution characteristics of the real pores into account, and applied to reconstruct the microstructure of micron silver sintered joints under thermal shock test conditions and transferred into an FEA model. The comparison of autocorrelation functions characterizing morphology features of SEM images and reconstructed models proves this method is feasible.
- (2) A simulation process based on the reconstructed model is proposed to obtain the effective elastic modulus of sintered joints. Through comparing the result with that of analytical models and nanoindentation tests, the relative error (less than 15%) indicates the rationality of this method.
- (3) The microstructural evolution is quantitatively characterized by autocorrelation functions. In the simulative deep space environment, with increasing thermal shocks, the average micron-silver particle size and hydraulic diameter decrease, while the specific surface goes up, resulting in the increase in porosity and dispersion of silver grains.

- (4) The FEA simulation results show that, due to the sandwich sample structure, the constrained sintering state makes the sintered silver joints present a slight anisotropy, which is reflected in the differences of displacement, stress and elastic modulus among X, Y, and Z directions. As thermal shock cycles increase, the material densification declines, resulting in the decreased apparent density, a larger displacement field across the local bearing surface, and more likely stress concentrations.
- (5) Elasticity degradation is noticed during the thermal shock test. The mechanism analysis shows accumulated thermal shocks lead to cyclic shear force in sintered joints, which induces lattice shift and dislocation slip in the microstructure. Furthermore, dislocation piling up causes the effective elastic modulus of sintered joints to decline due to broken atomic bonds.

Author Contributions: Conceptualization, B.W.; methodology, W.G.; software, W.G.; validation, W.G. and B.W.; formal analysis, W.G.; investigation, G.F.; resources, G.F.; data curation, M.Z.; writing—original draft, W.G.; writing—review and editing, B.W.; visualization, W.G.; supervision, G.F.; funding acquisition, M.Z. All authors have read and agreed to the published version of the manuscript.

Funding: The research was funded by the Equipment Pre-research Fund Project in China, grant number 61400020105.

Acknowledgments: The authors would thank the Institute of Microelectronics, Chinese Academy of Sciences for its assistance in making samples.

Conflicts of Interest: The authors declare no conflict of interest.

References

1. Ramesham, R. Reliability of tin-lead and lead-free solders of surface mounted miniaturized passive components for extreme temperature space missions. In Proceedings of the 41st International Conference on Environmental Systems 2011 (ICES 2011), Portland, Oregon, 17–21 July 2011; GarciaBlanco, S., Ramesham, R., Eds.; Spie-Int Soc Optical Engineering: Bellingham, WA, USA, 2011; Volume 7928.
2. Li, Y.; Fu, G.; Wan, B.; Jiang, M.; Zhang, W.; Yan, X. Failure analysis of sac305 ball grid array solder joint at extremely cryogenic temperature. *Appl. Sci.* **2020**, *10*, 1951. [[CrossRef](#)]
3. Regalado, I.L.; Williams, J.J.; Joshi, S.; Dede, E.M.; Liu, Y.; Chawla, N. X-Ray Microtomography of Thermal Cycling Damage in Sintered Nano-Silver Solder Joints. *Adv. Eng. Mater.* **2019**, *21*, 1–15. [[CrossRef](#)]
4. Zhang, H.; Chen, C.; Jiu, J.; Nagao, S.; Suganuma, K. High-temperature reliability of low-temperature and pressureless micron Ag sintered joints for die attachment in high-power device. *J. Mater. Sci. Mater. Electron.* **2018**. [[CrossRef](#)]
5. Knoerr, M.; Kraft, S.; Schletz, A. Reliability assessment of sintered nano-silver die attachment for power semiconductors. In Proceedings of the 2010 12th Electronics Packaging Technology Conference (EPTC 2010), Singapore, 8–10 December 2010; pp. 56–61. [[CrossRef](#)]
6. Zhao, Z.; Zhang, H.; Zou, G.; Ren, H.; Zhuang, W.; Liu, L.; Zhou, Y.N. A Predictive Model for Thermal Conductivity of Nano-Ag Sintered Interconnect for a SiC Die. *J. Electron. Mater.* **2019**, *48*, 2811–2825. [[CrossRef](#)]
7. Zhang, H.; Wang, W.; Bai, H.; Zou, G.; Liu, L.; Peng, P.; Guo, W. Microstructural and mechanical evolution of silver sintering die attach for SiC power devices during high temperature applications. *J. Alloy. Compd.* **2019**, *774*, 487–494. [[CrossRef](#)]
8. Sun, Z.; Wang, Z.; Qian, C.; Ren, Y.; Feng, Q.; Yang, D.; Sun, B. Characterization of stochastically distributed voids in sintered nano-silver joints. In Proceedings of the 2019 20th International Conference on Thermal, Mechanical and Multi-Physics Simulation and Experiments in Microelectronics and Microsystems, (EuroSimE 2019), Hannover, Germany, 24–27 March 2019; pp. 1–6. [[CrossRef](#)]
9. Fu, S.; Mei, Y.; Li, X.; Ma, C.; Lu, G.Q. Reliability Evaluation of Multichip Phase-Leg IGBT Modules Using Pressureless Sintering of Nanosilver Paste by Power Cycling Tests. *IEEE Trans. Power Electron.* **2017**, *32*, 6049–6058. [[CrossRef](#)]
10. Okereke, M.I.; Ling, Y. A computational investigation of the effect of three-dimensional void morphology on the thermal resistance of solder thermal interface materials. *Appl. Therm. Eng.* **2018**, *142*, 346–360. [[CrossRef](#)]

11. Jiang, C.; Fan, J.; Qian, C.; Zhang, H.; Fan, X.; Guo, W.; Zhang, G. Effects of voids on mechanical and thermal properties of the die attach solder layer used in high-power LED chip-scale packages. *IEEE Trans. Compon. Packag. Manuf. Technol.* **2018**, *8*, 1254–1262. [[CrossRef](#)]
12. Zhu, L.; Xu, Y.; Zhang, J.; Liang, L.; Liu, Y. Reliability study of solder interface with voids using an irreversible cohesive zone model. In Proceedings of the 16th International Conference on Electronic Packaging Technology (ICEPT 2015), Changsha, China, 11–14 August 2015; pp. 915–920. [[CrossRef](#)]
13. Youssef, T.; Rmili, W.; Woïrgard, E.; Azzopardi, S.; Vivet, N.; Martineau, D.; Meuret, R.; Le Quilliec, G.; Richard, C. Power modules die attach: A comprehensive evolution of the nanosilver sintering physical properties versus its porosity. *Microelectron. Reliab.* **2015**, *55*, 1997–2002. [[CrossRef](#)]
14. Milhet, X.; Gadaud, P.; Caccuri, V.; Bertheau, D.; Mellier, D.; Gerland, M. Influence of the Porous Microstructure on the Elastic Properties of Sintered Ag Paste as Replacement Material for Die Attachment. *J. Electron. Mater.* **2015**, *44*, 3948–3956. [[CrossRef](#)]
15. Torquato, S. Microstructural Descriptors. In *Random Heterogeneous Materials*; Springer: New York, NY, USA, 2002; pp. 23–58. [[CrossRef](#)]
16. Malmir, H.; Sahimi, M.; Jiao, Y. Higher-order correlation functions in disordered media: Computational algorithms and application to two-phase heterogeneous materials. *Phys. Rev. E* **2018**. [[CrossRef](#)]
17. Izadi, H.; Baniassadi, M.; Hormozzade, F.; Dehnavi, F.N.; Hasanabadi, A.; Memarian, H.; Soltanian-Zadeh, H. Effect of 2D Image Resolution on 3D Stochastic Reconstruction and Developing Petrophysical Trend. *Transp. Porous Media* **2018**. [[CrossRef](#)]
18. Safdari, M.; Baniassadi, M.; Garmestani, H.; Al-Haik, M.S. A modified strong-contrast expansion for estimating the effective thermal conductivity of multiphase heterogeneous materials. *J. Appl. Phys.* **2012**. [[CrossRef](#)]
19. Jiao, Y.; Stillinger, F.H.; Torquato, S. A superior descriptor of random textures and its predictive capacity. *Proc. Natl. Acad. Sci. USA* **2009**, *106*, 17634–17639. [[CrossRef](#)]
20. Izadi, H.; Baniassadi, M.; Hasanabadi, A.; Mehrgini, B.; Memarian, H.; Soltanian-Zadeh, H.; Abrinia, K. Application of full set of two point correlation functions from a pair of 2D cut sections for 3D porous media reconstruction. *J. Pet. Sci. Eng.* **2017**, *149*, 789–800. [[CrossRef](#)]
21. Tewari, A.; Gokhale, A.M.; Spowart, J.E.; Miracle, D.B. Quantitative characterization of spatial clustering in three-dimensional microstructures using two-point correlation functions. *Acta Mater.* **2004**, *52*, 307–319. [[CrossRef](#)]
22. Wang, Q.; Zhang, H.; Cai, H.; Fan, Q.; Li, G. Reconstruction of co-continuous ceramic composites three-dimensional microstructure solid model by generation-based optimization method. *Comput. Mater. Sci.* **2016**. [[CrossRef](#)]
23. Muhumthan, B. New three-dimensional modeling technique for studying porous media. *J. Colloid Interface Sci.* **1993**, *98*, 228–235. [[CrossRef](#)]
24. Bodla, K.K.; Garimella, S.V.; Murthy, J.Y. 3D reconstruction and design of porous media from thin sections. *Int. J. Heat Mass Transf.* **2014**, *73*, 250–264. [[CrossRef](#)]
25. Ramakrishnan, N.; Arunachalam, V.S. Effective elastic moduli of porous solids. *J. Mater. Sci.* **1990**, *25*, 3930–3937. [[CrossRef](#)]
26. Roberts, A.P.; Garboczi, E.J. Elastic properties of a tungsten-silver composite by reconstruction and computation. *J. Mech. Phys. Solids* **1999**, *47*, 2029–2055. [[CrossRef](#)]
27. Yeong, C.L.Y.; Torquato, S. Reconstructing Random Media I and II. *Phys. Rev. E* **1998**, *58*, 224–233. [[CrossRef](#)]
28. Dullien, F.A.L. *Porous Media: Fluid Transport and Pore Structure*; Academic Press: San Diego, CA, USA, 1979; ISBN 0122236505.
29. Nishimoto, S.; Moeini, S.A.; Ohashi, T.; Nagatomo, Y.; McCluskey, P. Novel silver die-attach technology on silver pre-sintered DBA substrates for high temperature applications. *Microelectron. Reliab.* **2018**, *87*, 232–237. [[CrossRef](#)]
30. Asoro, M.A.; Ferreira, P.J.; Kovar, D. In situ transmission electron microscopy and scanning transmission electron microscopy studies of sintering of Ag and Pt nanoparticles. *Acta Mater.* **2014**, *81*, 173–183. [[CrossRef](#)]

31. Kim, D.; Chen, C.; Pei, C.; Zhang, Z.; Nagao, S.; Suetake, A.; Sugahara, T.; Suganuma, K. Thermal shock reliability of a GaN die-attach module on DBA substrate with Ti/Ag metallization by using micron/submicron Ag sinter paste. *Jpn. J. Appl. Phys.* **2019**, *58*. [[CrossRef](#)]
32. Wang, X.; Atkinson, A. Microstructure evolution in thin zirconia films: Experimental observation and modelling. *Acta Mater.* **2011**. [[CrossRef](#)]



© 2020 by the authors. Licensee MDPI, Basel, Switzerland. This article is an open access article distributed under the terms and conditions of the Creative Commons Attribution (CC BY) license (<http://creativecommons.org/licenses/by/4.0/>).